

Article

Na₂WO₄/Mn/SiO₂ Catalyst Pellets for Upgrading H₂S-Containing Biogas via the Oxidative Coupling of Methane

Sangseo Gu ^{1,2} , Jae-Wook Choi ², Dong Jin Suh ^{2,3}, Chun-Jae Yoo ² , Jungkyu Choi ^{1,*} and Jeong-Myeong Ha ^{2,4,*} 

¹ Department of Chemical and Biological Engineering, Korea University, Seoul 02841, Korea; tjfntkd@korea.ac.kr

² Clean Energy Research Center, Korea Institute of Science and Technology, Seoul 02792, Korea; choijw@kist.re.kr (J.-W.C.); djsuh@kist.re.kr (D.J.S.); cjyoo@kist.re.kr (C.-J.Y.)

³ Graduate School of Energy and Environment (Green School), Korea University, Seoul 02841, Korea

⁴ Division of Energy and Environment Technology, KIST School, Korea University of Science and Technology, Seoul 02792, Korea

* Correspondence: jungkyu_choi@korea.ac.kr (J.C.); jmha@kist.re.kr (J.-M.H.); Tel.: +82-2-3290-4854 (J.C.); +82-2-958-5837 (J.-M.H.)

Abstract: Biogas is a promising renewable energy source; however, it needs to be upgraded to increase its low calorific value. In this study, oxidative coupling of methane (OCM) was selected to convert it to a higher fuel standard. Prior to establishing the scaled-up OCM process, the effect of organic/inorganic binders on catalytic activity was examined. The selection of the binders and composition of the catalyst pellet influenced the pore structure, fracture strength, and catalytic activity of the catalyst pellets. It was also observed that the O₂ supply from the inorganic binder is a key factor in determining catalytic activity, based on which the composition of the catalyst pellets was optimized. The higher heating value increased from 39.9 (CH₄, Wobbe index = 53.5 MJ/Nm³) to 41.0 MJ/Nm³ (OCM product mixture, Wobbe index = 54.2 MJ/Nm³), achieving the fuel standard prescribed in many countries (Wobbe index = 45.5–55.0 MJ/Nm³). The reaction parameters (temperature, gas hourly space velocity, size of the reaction system, and the CH₄/O₂ ratio) were also optimized, followed by a sensitivity analysis. Furthermore, the catalyst was stable for a long-term (100 h) operation under the optimized conditions.

Keywords: heterogeneous catalysts; biogas conversion; tube-shaped catalyst pellets; high sulfur-compound resistance



Citation: Gu, S.; Choi, J.-W.; Suh, D.J.; Yoo, C.-J.; Choi, J.; Ha, J.-M. Na₂WO₄/Mn/SiO₂ Catalyst Pellets for Upgrading H₂S-Containing Biogas via the Oxidative Coupling of Methane. *Catalysts* **2021**, *11*, 1301. <https://doi.org/10.3390/catal11111301>

Academic Editor: Joris W. Thybaut

Received: 6 October 2021

Accepted: 18 October 2021

Published: 28 October 2021

Publisher's Note: MDPI stays neutral with regard to jurisdictional claims in published maps and institutional affiliations.



Copyright: © 2021 by the authors. Licensee MDPI, Basel, Switzerland. This article is an open access article distributed under the terms and conditions of the Creative Commons Attribution (CC BY) license (<https://creativecommons.org/licenses/by/4.0/>).

1. Introduction

Biogas is a renewable energy source produced through the anaerobic digestion of organic wastes, which can be used to produce heat and electricity [1–3]. Replacing fossil fuels with sustainable biogas can reduce greenhouse gas emissions [4–6]; therefore, the global demand for biogas is growing [7,8]. Biogas is a mixture of CH₄, CO₂, H₂, H₂S, and other compounds, and its composition depends on feedstock and digestion conditions [9,10]. Biologically produced CH₄, a major component of biogas, has been purified or upgraded to replace natural gas, i.e., cleaning (removing unwanted compounds) and upgrading (increasing the heating value of biogas) have been attempted [2,11,12]. The mass production of biogas is globally achieved typically for heat generation, and the valorization of biogas into high-quality fuels and chemical feedstocks can also be performed to replace the current fossil fuel-based conventional chemical industry.

Among the possible methods of upgrading, oxidative coupling of methane (OCM) has been proposed to be promising for improving the heating value of biogas and produce valuable chemical feedstocks [13–16]. The OCM converts CH₄ to C₂ or higher carbon number hydrocarbons (C₂₊ compounds), which have heating values two or three times higher

than CH₄ (Table S1), to meet global fuel standards (Wobbe index = 45.5–55.0 MJ/Nm³). However, the OCM is highly exothermic ($\Delta H = -87$ kJ/mol at 800 °C) and requires an O₂ reactant, producing unwanted byproducts in excess, including CO and CO₂ (CO_x).

For selectively producing paraffins and olefins via OCM, many catalysts have been reported [17,18]. The Na₂WO₄/Mn/SiO₂ (NWM) catalyst is particularly advantageous because of its high activity and stability [19–27]. In addition to its application in upgrading natural gas, the economically feasible upgrading of biogas via OCM using NWM has been suggested [13–15], which exhibits high sulfur resistance and high stability for a long-term OCM process using a simulated H₂S-containing biogas reactant [16]. Based on the feasibility of OCM for biogas observed at the lab scale, its possible scale-up to the industrial scale has been investigated with a typical OCM using a methane reactant in our lab [28].

In an industrial process, the catalyst pellets in small, compressed, and hard chunk forms are used for the efficient operation of large-scale processes. Mechanical rigidity is a key parameter in a catalyst pellet because the abrasion of catalyst pellets results in a significant pressure drop, and the resulting overheating of a reactor creates low efficiency and a consequent plant shutdown [29].

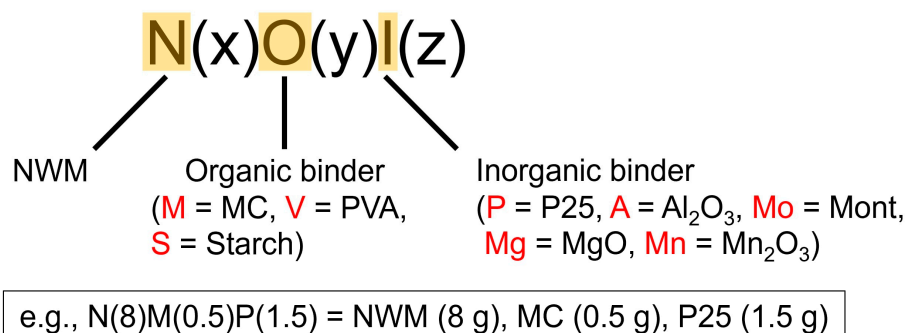
In this study, OCM using NWM catalyst pellets to upgrade biogas was investigated to (i) elucidate the effects of the catalyst pellets on OCM activity and (ii) optimize the reaction conditions. Catalyst pellets containing NWM, one of the most stable and active OCM catalysts, were used for biogas conversion [22]. The mechanically stable catalyst pellets were prepared using an extrusion method. This manuscript will investigate whether the geometric (pore structure and mechanical strength) and electronic properties of the prepared catalyst pellets are highly dependent on organic and inorganic binders, as illustrated in the literature [30–32]. The composition and types of binders can be manipulated to achieve optimal OCM activity [29,33]. Additionally, the organic binders induce the formation of pore structures, whose removal by calcination creates spaces between the catalyst powder particles and disperses the active sites on the catalyst pellets. However, the use of organic binders may not influence catalytic activity if the pore structures collapse during high-temperature calcination typically used for OCM catalysts [34–36]. Further, the addition of inorganic binders can improve the mechanical strength of the pellets. The inorganic binders of metals or metal oxides can also manipulate the electronic states of the active components by supplying oxygen to the OCM catalyst systems [37–42]. The OCM using catalyst pellets can also be controlled by reactor design and operating conditions [37,43,44] because the catalysis results are highly dependent on the reaction conditions [44–47]. Finally, optimization of the gas hourly space velocity (GHSV), reaction temperature, reactant flow rate, and CH₄/O₂ ratio was performed to determine the feasible operating range for the desired OCM activity represented by C₂₊ selectivity, olefin selectivity, and C₂₊ yield.

2. Results and Discussion

2.1. Preparation of Catalyst Pellets and Their Physical Properties

The pore structures and mechanical strength of the catalyst pellets are important for the reaction. This is because the pore structures can adjust the mass and heat transfer in the catalyst bed to manipulate catalytic activity, while brittle pellets cannot be used for industry-scale reaction processes; therefore, a high mechanical strength is required. To prepare the catalyst pellets in this study, organic binders, including methyl cellulose (MC or M), polyvinyl chloride (PVA or V), and starch, as well as inorganic binders, including TiO₂ P25 (P25 or P), Al₂O₃ (A), montmorillonite (Mont or Mo), MgO (Mg), and Mn₂O₃ (Mn), were mixed, and the physical properties of the prepared pellets were characterized prior to the OCM reaction (fresh catalyst pellets). The nomenclature used to refer to the catalyst pellets is described in Scheme 1. The effects of the organic binders, with P25 as the inorganic binder, on the pore structures and mechanical properties of the catalyst pellets were investigated by measuring their Brunauer–Emmett–Teller (BET) surface area and fracture strength (Table 1). For the MC, PVA, and starch binders with an inorganic binder P25, negligible BET surface areas (1–2 m²/g) were obtained, indicating the collapse of

the pores during high-temperature calcination [34–36]. For pellets containing the organic binder MC and different inorganic binders, BET surface areas of 1–8 m²/g were obtained. Notably, the measured BET surface areas of the catalyst pellets in this study were not significantly different from those of the catalyst powder (3 m²/g), indicating that the pore formation in the pellets was not particularly significant during pelletization. The largest BET surface area (8 m²/g) was observed for N(80)M(15)A(15), a pellet containing MC (organic binder) and Al₂O₃ (inorganic binder); this was attributed to the high BET surface area of Al₂O₃.



Scheme 1. Nomenclature of NWM pellets.

Table 1. Physical properties of the catalyst pellets ^a.

Catalyst	Fracture Strength (MPa)	BET Surface Area (m ² /g)
NWM (Powder)	n.a.	3
Using organic binder of MC		
N(8)M(0.5)	1.45	2
N(8)M(0.5)P(1.5)	2.79	2
N(80)M(5)A(5)	0.54	8
N(8)M(0.5)Mo(1.5)	0.19	2
N(8)M(0.5)Mg(1.5)	0.42	2
N(8)M(0.5)Mn(1.5)	0.40	1
Using inorganic binder of P25		
N(8)M(0.5)P(1.5)	2.79	2
N(8)V(0.5)P(1.5)	2.65	2
N(8)S(0.5)P(1.5)	2.52	1

^a NWM or N: Na₂WO₄/Mn/SiO₂; M: MC, or methyl cellulose; P: TiO₂ P25 or P25; A: Al₂O₃; Mo: montmorillonite or Mont; Mg: MgO; Mn: Mn₂O₃; P: PVA; S: starch.

When inorganic binder P25 was mixed with organic binders MC, PVA, and starch, a minimal change in the fracture strength of the catalyst pellets was observed (2.52–2.79 MPa), as compared to that of N₈₀M₅P₁₅ (2.79 MPa). However, adding other inorganic binders (Mont, Mn₂O₃, MgO, and Al₂O₃) with organic binder MC significantly reduced the fracture strength (0.19–1.45 MPa). These observations indicate that the inorganic binder is the highest contributing factor toward the fracture strength of the pellets, and P25 is the optimum inorganic binder to produce pellets with the highest mechanical stability. Observations of the BET surface area and fracture strength also suggest that the organic binders help pelletize the powder particles, but do not significantly impact the physical properties upon removal during calcination.

Scanning electron microscopy (SEM) images of the prepared pellets exhibited different surface morphologies depending on the inorganic binder (Figure 1). In the absence of inorganic binder (N(8)M(0.5)), which contained only the NWM catalyst after the organic binder was removed during calcination, the pellet formed large particles networked with others. Adding inorganic binders P25, Mont, MgO, and Mn₂O₃ did not significantly change surface morphology. However, adding Al₂O₃ led to the formation of small sub-micrometer

particles on the surface, which may be small OCM-inert Al_2O_3 particles. Barring the presence of small particles on the surface, the near-identical morphology of the pellets suggests that the mass and heat transfer in the catalyst pellets may not be influenced by the type of inorganic binder.

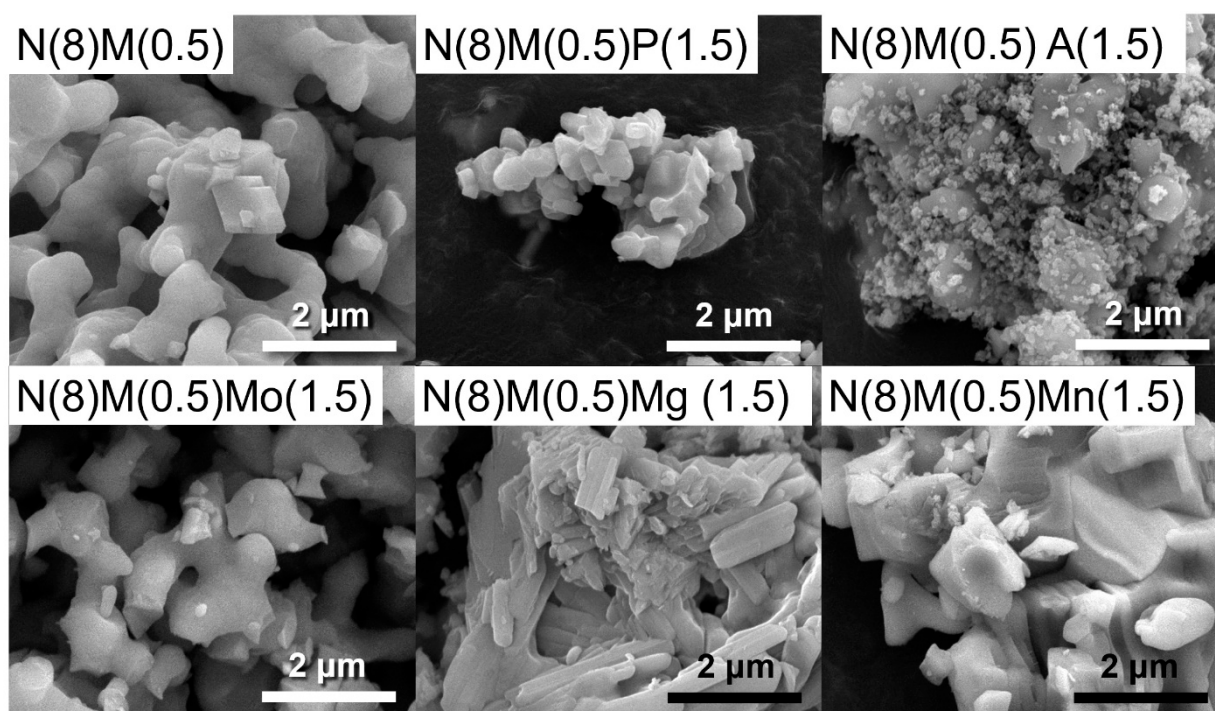


Figure 1. SEM images of the catalyst pellets prepared using an organic binder MC and different inorganic binders.

Organic binder MC and inorganic binder P25 were selected based on the observed physical properties of the catalyst pellets. Because the organic binder was used for agglomerating the catalyst powder only, and not for manipulating the physical properties of the pellets, optimization of the P25 fraction was performed (Table 2). The highest fracture strength of the catalyst pellets was observed for 15 wt % P25 or N(8)M(0.5)P(1.5), while N(8)P(1.5) prepared without the organic binders exhibited the lowest BET surface area. A lower surface area may correlate with reduced catalytic activity and poor mass transport (Table 2). However, because the pore structure collapses during calcination, adjusting the amount of organic binder does not significantly change the BET surface area.

Table 2. Physical properties of catalyst pellets containing MC and P25.

Catalyst	Fracture Strength (MPa)	BET Surface Area (m^2/g)
N(8)M(0.5)	1.45	2
M(8)M(0.5)P(0.75)	1.60	2
N(8)M(0.5)P(1.5)	2.79	2
N(8)M(0.5)P(3)	2.57	3
N(8)M(0.5)P(6)	2.23	3
N(8)P(1.5)	0.29	1
N(8)M(0.25)P(1.5)	1.72	2
N(8)M(0.5)P(1.5)	2.79	2
N(8)M(1)P(1.5)	0.43	2
N(8)M(2)P(1.5)	0.29	2

2.2. Biogas Upgrading Using Catalyst Pellets

An OCM of the biogas-simulating mixture composed of CH₄, O₂, N₂, CO₂, and H₂S was performed using the prepared catalyst pellets (Tables 3 and S2). The OCM activity did not significantly change depending on the type of organic binder (Table S3), and the effects of the inorganic binders were the focus of this study. Compared to the NWM powder catalyst, the catalyst pellet without an inorganic binder (N(8)M(0.5)) exhibited a lower CH₄ conversion (8.20% to 7.85%) and C₂₊ selectivity (63.5% to 51.0%). The absence of the inorganic binders enables the channeling of the reactants through the void space between the pellets. Further, the dehydrogenation of paraffins to olefins was also suppressed, exhibiting lower olefin selectivity (28.5% to 21.0%).

Table 3. OCM results of simulated biogas at 800 °C using catalyst pellets with different inorganic binders ^a.

Catalyst	Methane Conversion (%)	C ₂₊ Selectivity (%) ^b	Olefin Selectivity (%) ^c	C ₂₊ Yield (%) ^b	Olefin/Paraffin (mol/mol) ^d	O ₂ Conversion (%)	HHV (MJ/Nm ³) ^e
NWM (Powder)	8.20	63.5	28.5	5.09	0.82	66.7	40.6
N(8)M(0.5)	7.85	51.0	21.0	3.99	0.70	65.4	40.4
N(8)M(0.5)P(1.5)	10.0	83.9	44.4	8.39	1.12	77.8	41.0
N(8)M(0.5)A(1.5)	3.43	49.0	16.7	1.68	0.52	59.2	40.1
N(8)M(0.5)Mo(1.5)	6.00	33.3	11.0	1.95	0.50	56.6	40.1
N(8)M(0.5)Mg(1.5)	7.76	28.9	10.5	2.19	0.58	65.9	40.2
N(8)M(0.5)Mn(1.5)	8.63	71.7	34.9	6.19	0.95	70.6	40.7

^a Reaction conditions: GHSV = 10,000 h⁻¹, 0.18 mL of catalyst, 800 °C, 30 mL/min of flow rate composed of CH₄/O₂/N₂/CO₂/H₂S = 16.1/2/1/10.7/0.1 (v/v/v/v/v). ^b C₂₊ indicates paraffins and olefins including ethane, ethylene, propane, propylene, and other hydrocarbons with higher carbon numbers. ^c Olefin contains ethylene and propylene. ^d Paraffin contains ethane and propane. ^e 0 °C, 1 atm.

For the pellets containing organic binder MC and inorganic binders Al₂O₃, Mont, or MgO, poor OCM activity was observed (low CH₄ conversion, low C₂₊ selectivity, and low C₂₊ yield). Furthermore, MgO alone exhibited a high C₂₊ selectivity (Table S4), whereas its mixture with NWM did not. However, pellets with inorganic binders P25 (N(8)M(0.5)P(1.5)) and Mn₂O₃ (N(8)M(0.5)Mn(1.5)) exhibited higher OCM activity compared to the NWM powder: CH₄ conversion (7.85% to 10.0% and 8.63%, respectively) and C₂₊ selectivity (51.0% to 83.9% and 71.7%, respectively); however, it is to be noted that the pellets contained less NWM because of the inorganic binder fraction. The improved catalytic activity with the addition of P25 and Mn₂O₃ can be attributed to the improved O₂ supply [37–39].

From the above results, the catalyst pellets containing P25 exhibit the highest catalytic activity. Thus, the effect of P25 content on OCM activity was studied (Table 4). CH₄ conversion, O₂ conversion, and C₂₊ yield increased with increasing P25 fraction; however, as stated above, increasing the P25 fraction decreases the fraction of OCM-active NWM. N(55)M(4)P(41), with the largest fraction of P25 in this study, exhibited the highest CH₄ conversion (12.8%) and O₂ conversion (95.5%). However, C₂₊ selectivity decreased with the increasing P25 fraction, indicating that the conversion of methane to paraffins and olefins decreased with decreasing fractions of OCM-active NWM. Dehydrogenation was also favored, with an increasing fraction of P25. The highest C₂₊ selectivity (83.9%) and highest olefin selectivity (44.4%) were achieved for N(8)M(0.5)P(1.5).

In addition to the inorganic binders, the effect of varying the organic binder content on OCM activity was also determined. However, this was less significant with adjusting the MC-to-NWM ratio to 0–2/8 (w/w), exhibiting 10.0–11.5% CH₄ conversion, 73.1–83.9% C₂₊ selectivity, and 7.81–8.66% C₂₊ yield (Table 4). Notably, N(8)M(0.5)P(1.5) exhibited the highest C₂₊ selectivity (83.9%) and olefin selectivity (44.4%). However, in the absence of organic binder MC(N(8)P(1.5)), a lower CH₄ conversion (5.72%) and a lower C₂₊ selectivity (67.7%) were observed, indicating that, despite its less significant manipulation of the catalyst structure, an organic binder is required for improved inorganic binder-induced OCM activity.

Table 4. OCM results of simulated biogas at 800 °C using catalyst pellet depending on the composition of the inorganic and organic binders ^a.

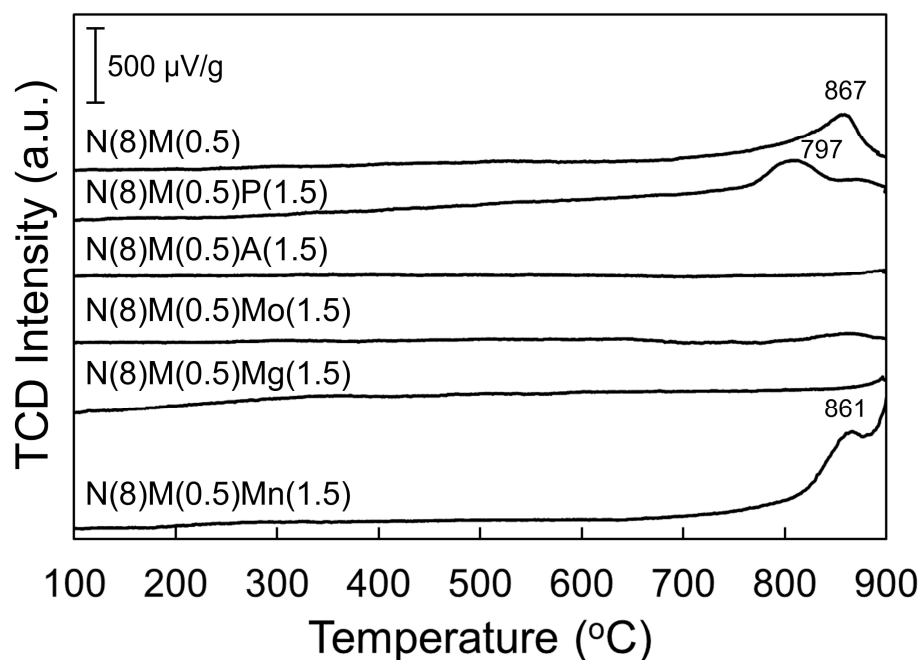
Catalyst	Methane Conversion (%)	C ₂₊ Selectivity (%) ^b	Olefin Selectivity (%) ^c	C ₂₊ Yield (%) ^b	Olefin/Paraffin (mol/mol) ^d	O ₂ Conversion (%)	HHV (MJ/Nm ³) ^e
N(8)M(0.5)	7.85	51.0	21.0	3.99	0.70	65.4	40.4
M(8)M(0.5)P(0.75)	9.51	81.5	42.6	7.75	1.10	79.2	40.9
N(8)M(0.5)P(1.5)	10.0	83.9	44.4	8.39	1.12	77.8	41.0
N(8)M(0.5)P(3)	11.5	77.2	41.9	8.80	1.18	85.4	41.1
N(8)M(0.5)P(6)	12.8	73.6	40.6	9.36	1.23	95.5	41.2
N(8)P(1.5)	5.72	67.7	29.0	3.83	0.75	65.7	40.4
N(8)M(0.25)P(1.5)	10.3	80.3	42.4	8.26	1.12	86.8	41.0
N(8)M(0.5)P(1.5)	10.0	83.9	44.4	8.39	1.12	77.8	41.0
N(8)M(1)P(1.5)	11.5	75.2	40.7	8.66	1.18	78.2	41.1
N(8)M(2)P(1.5)	10.7	73.1	38.2	7.81	1.09	74.3	41.0

^a Reaction conditions: GHSV = 10,000 h⁻¹, 0.18 mL of catalyst, 800 °C, 30 mL/min of flow rate composed of CH₄/O₂/N₂/CO₂/H₂S = 16.1/2/1/10.7/0.1 (v/v/v/v/v). ^b C₂₊ indicates paraffins and olefins including ethane, ethylene, propane, propylene, and other hydrocarbons with higher carbon numbers. ^c Olefin contains ethylene and propylene. ^d Paraffin contains ethane and propane. ^e 0 °C, 1 atm.

2.3. Catalyst Characterization

2.3.1. O₂ Temperature-Programmed Desorption (O₂ TPD)

O₂ TPD of a fresh (as-prepared) catalyst pellet was performed to elucidate the role of the inorganic binders in supplying O₂ to the reaction system (Figure 2). Among the pellets containing inorganic binders, N(8)M(0.5)P(1.5) and N(8)M(0.5)Mn(1.5), which exhibited good OCM activity, exhibited strong O₂ desorption peaks at 750 °C and above. Compared to the pellets without inorganic binders (N(8)M(0.5)), the O₂ desorption peaks of those containing P25 and Mn₂O₃ decreased (867 to 797 and 861 °C, respectively), indicating an easier oxygen supply from these inorganic binders [37,40].

**Figure 2.** O₂ temperature-programmed desorption results of fresh catalyst pellets containing different inorganic binders.

For the pellets containing inorganic binder P25, the O₂ desorption temperature varied with the P25 fraction (Figure S1). Increasing the fraction of P25 resulted in a higher

desorption temperature with a lower desorption peak intensity, indicating a suppressed oxygen supply. These observations indicate that the oxygen supply in the catalyst is manipulated by the presence of inorganic binder P25. Smaller fractions of P25 improved the oxygen supply, while an excess P25 suppressed it. An excess amount of P25 rapidly oxidizes the reactant, which can overwhelm the NWM-catalyzed OCM activity. For the catalyst pellet without organic binder MC (N(8)P(1.5)), the O₂ desorption temperature increased to 867 °C, which was higher than that of pellets containing organic binder MC (Figure S1). These observations confirm that both organic and inorganic binders are required for improved OCM activity of the catalyst pellets; the organic binder MC improves the contact between inorganic binder P25 and the NWM catalyst.

2.3.2. Powder X-ray Diffraction (Powder XRD)

Fresh catalyst pellets, calcined at 800 °C, exhibited the crystal structures of α -cristobalite (PDF#39-1425), Na₂WO₄ (PDF#12-0722), and Mn₇SiO₁₂ (PDF#41-1367) regardless of the binder (Figure 3a). The type of organic binder did not induce any significant changes in the crystalline structure of the pellet (Figure S2). However, the formation of quartz (PDF #46-1045) was observed with the addition of the inorganic binders P25, Mont, MgO, and Mn₂O₃, but not with Al₂O₃. Because the formation of cristobalite has been observed in silica supports of the NWM catalyst [34], and quartz was not observed in the absence of inorganic binders (N(8)M(0.5)), the presence of quartz can be attributed to the presence of the non-silica inorganic binders. Interestingly, the catalyst pellets containing P25, exhibiting the high diffraction peaks for quartz, achieved the highest OCM activity (Table 3), although the formation of cristobalite has been suggested to improve the OCM activity [22]. The formation of quartz was further investigated by calcining N(8)M(0.5)P(1.5) in air, N₂, and 5% H₂/Ar (Figure S3). While quartz formed in the oxidizing (air) and inert (N₂) environments, the formation of cristobalite was observed in the reducing (5% H₂/Ar) environment. These observations indicate that the oxidation of TiO₂ contributed to the formation of quartz. The possible oxygen supply from TiO₂ to the adjacent NWM may improve OCM activity, although the formation of cristobalite is suppressed with inorganic binder P25.

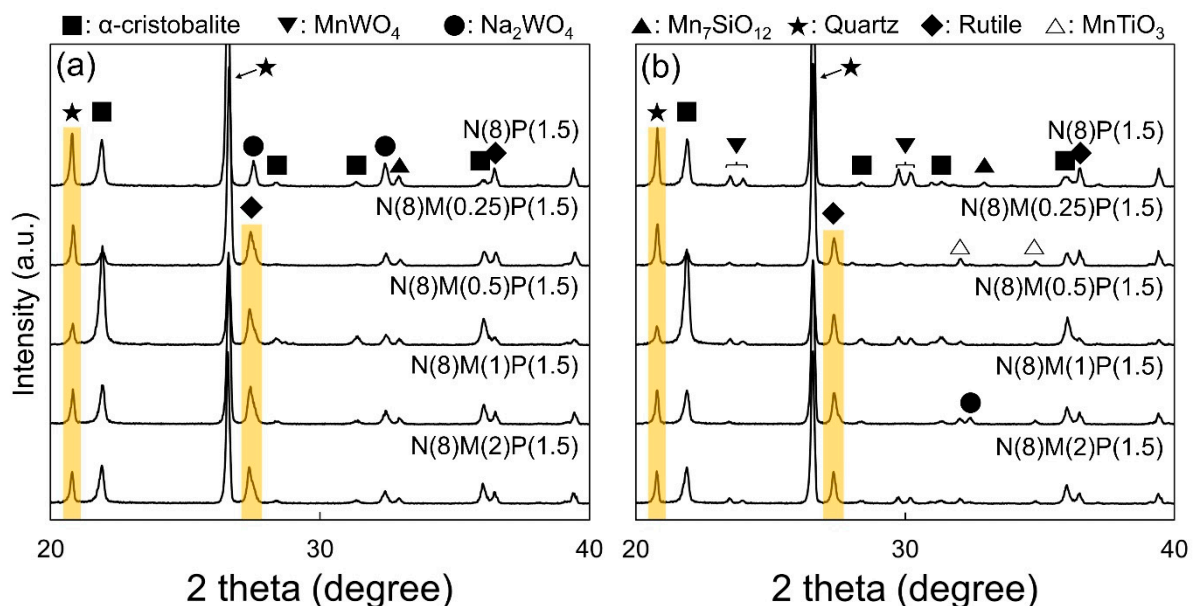


Figure 3. X-ray diffraction patterns of (a) fresh and (b) spent catalyst pellets depending on inorganic binders.

During the OCM reaction, the OCM-active Na_2WO_4 transformed into MnWO_4 (PDF#13-0434) (Figure 3b) because of the redox cycle that supplies oxygen atoms to the active WO_4 [43]. Active WO_4 as MnWO_4 was present in fresh N(8)M(0.5)A(1.5) and N(8)M(0.5)Mo(1.5), while fresh and spent N(8)M(0.5)Mg(1.5) exhibited the formation of MgWO_4 (PDF# 27-0789), which indicated a strong interaction between MgO and WO_4 , leading to lower OCM activity. Further, MnTiO_3 (PDF# 29-0902), which catalyzes O_2 activation at a lower temperature [38], was observed in spent N(8)M(0.5)P(1.5). The formation of MnTiO_3 was also confirmed by the TEM-EDS results (Figure S4).

The change in the catalyst structure during the OCM reaction was further investigated using high-temperature powder XRD measurements (Figure 4). With increasing temperature, a new SiO_2 phase, tridymite (PDF #42-1401), formed, and the peaks of cristobalite shifted to a lower 2θ because of its transition to β -cristobalite [48]. Quartz was still observed at high temperatures. Furthermore, a distinct change in the crystal structures of N(8)M(0.5)P(1.5) and N(8)M(0.5)Mn(1.5) with increasing temperature was observed. At 850°C , the MnWO_4 peaks decreased and the $\text{Mn}_7\text{SiO}_{12}$ peaks increased. Because MnWO_4 was favored under reductive conditions (Figure S3) and the oxidation state of Mn was higher in $\text{Mn}_7\text{SiO}_{12}$ (2+ and 3+) than in MnWO_4 (2+), the catalysts were oxidized at higher temperatures, while the redox cycle supplied oxygen to the active WO_4 [42]. The presence of isolated Mn and W, which do not form Mn-W oxides, suggests the formation of highly dispersed Na- WO_4 surface sites [27]. Therefore, the improved OCM activity of the catalyst pellets containing inorganic binders is attributed to the facile oxygen supply and the formation of new active sites (MnTiO_3); however, quartz does not promote OCM activity.

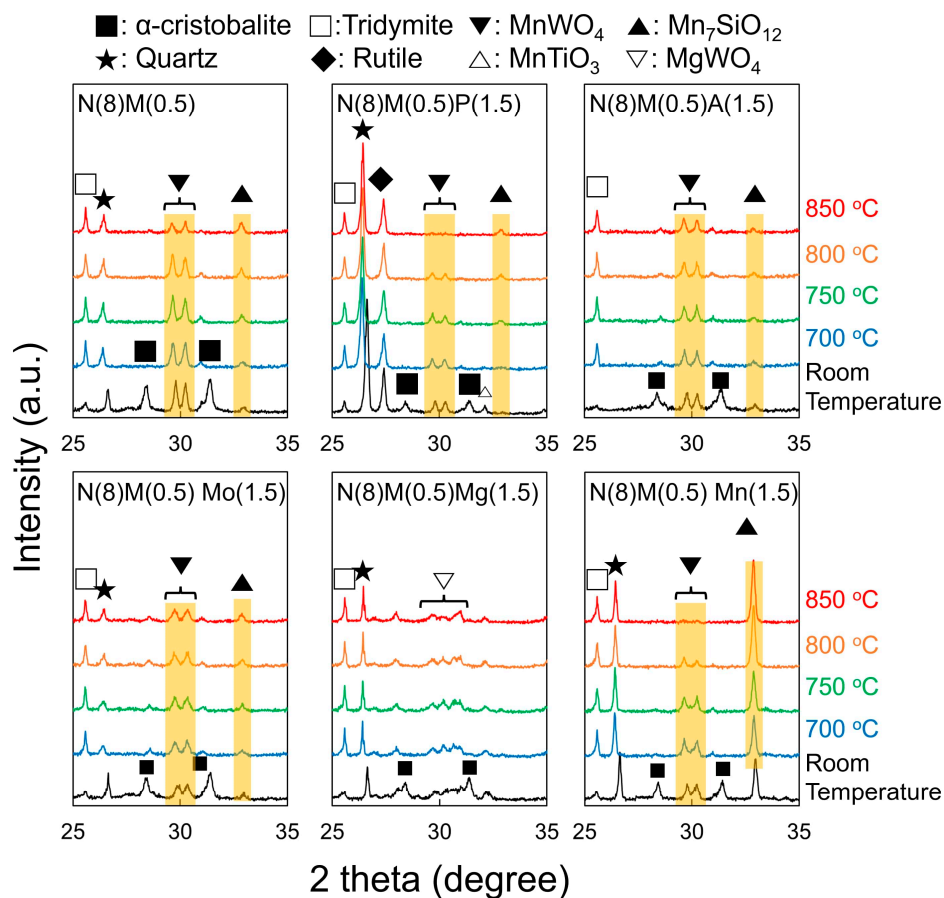


Figure 4. High temperature powder XRD results of spent catalysts.

The effect of P25 on the crystal structure of the catalyst pellets was also investigated (Figure S5). Without binder (N(8)M(0.5)), the silica support exhibited α -cristobalite with a low intensity peak of quartz. Adding P25 increased the peaks of quartz and rutile TiO_2 , while those of Na_2WO_4 , $\text{Mn}_7\text{SiO}_{12}$, and MnTiO_3 decreased. On the other hand, the type and amount of the organic binders did not significantly affect the crystal structure (Figures S2 and S5). Quartz was observed as a major phase for SiO_2 , but MnTiO_3 did not form in the absence of the organic binder. Since the organic binder acts as a glue for the inorganic binder and NWM, its absence limits their interaction, leading to the absence of MnTiO_3 .

2.3.3. Electronic Structures

The electronic structures of the NWM catalyst pellets were observed by X-ray photoelectron spectroscopy (XPS) (Figures 5 and S6–S10) [37–41]. The W 4f peaks of the fresh calcined N(8)M(0.5)P(1.5) and N(8)M(0.5)Al(1.5) did not exhibit a significant shift in the binding energy compared to that of the inorganic binder-free N(8)M(0.5), while those of N(8)M(0.5)Mo(1.5), N(8)M(0.5)Mg(1.5), and N(8)M(0.5)Mn(1.5) exhibited lower binding energies closer to that of WO_4 . After the OCM using H_2S -containing biogas, the W 4f peaks of N(8)M(0.5)P(1.5) and N(8)M(0.5)Al(1.5) did not significantly change, but those of N(8)M(0.5)Mo(1.5), N(8)M(0.5)Mg(1.5), and N(8)M(0.5)Mn(1.5) shifted to a higher binding energy. In particular, a significant shift in N(8)M(0.5)Mg(1.5) toward a higher binding energy was observed. These observations indicate that inorganic binders Mont, MgO , and Mn_2O_3 were significantly modified during the H_2S -containing OCM, which altered their influence on NWM. In contrast, the catalyst pellets without an inorganic binder and those containing P25 and Al_2O_3 did not exhibit a significant shift in the W 4f peaks, indicating fewer modifications in the catalyst pellets during the OCM. These observations indicated that the W in the catalyst pellets was significantly affected by the H_2S -containing OCM and transformed into electron-poor W, degrading their OCM activity.

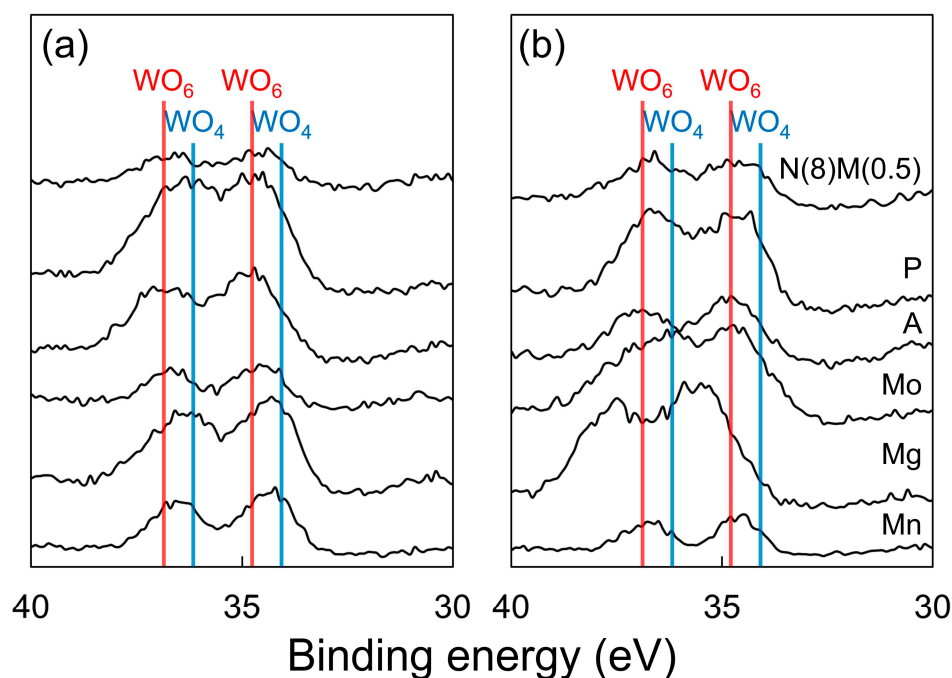


Figure 5. W 4f X-ray photoelectron spectroscopy results of (a) fresh and (b) spent catalyst pellets depending on the inorganic binders.

The binding energy of W $4f_{7/2}$ was between 34.6–35.6 eV with different inorganic binder while N(8)M(0.5) exhibited the binding energy of 34.7 eV. CH_4 conversion exhibited a weak relation with W $4f_{7/2}$ binding energy (Figure 6) because O_2 supply from the

inorganic binder modified the electronic structure of WO_4 tetrahedron [39]. The dependence demonstrates the oxidation activity of NWM catalyst can be modified by the O_2 supply from inorganic binder. $\text{N}(8)\text{M}(0.5)\text{Mg}(1.5)$ was deviated from the trend because of the strong interaction between MgO and WO_x .

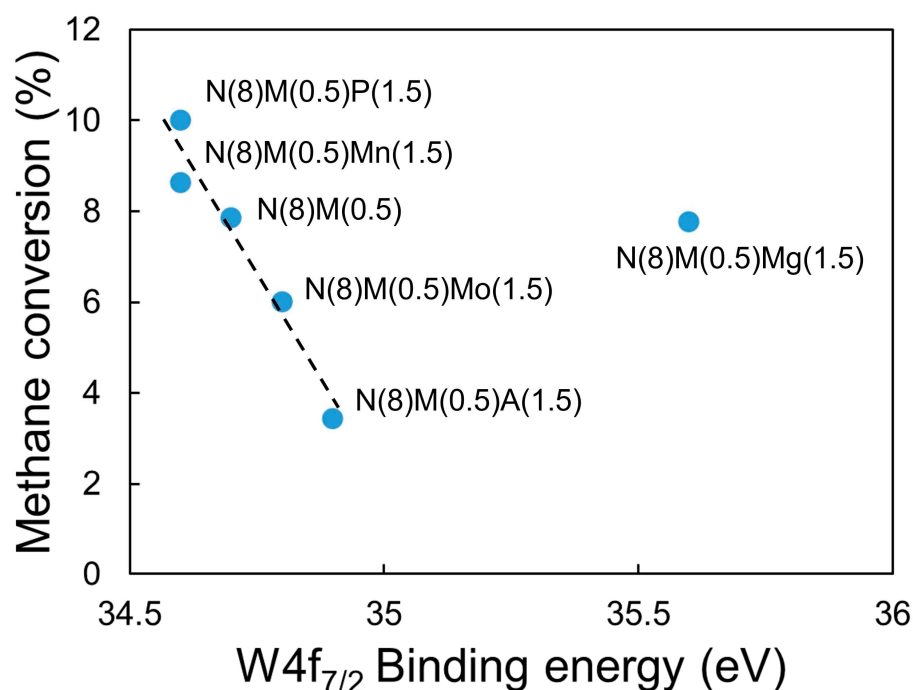


Figure 6. Correlation between W $4f_{7/2}$ binding energy of spent catalyst and methane conversion.

Furthermore, significant changes in the XPS results were observed for Na 1s (Mont), Si 2p (Mont, Mn_2O_3), and O 1s (Mont, Mn_2O_3) during the OCM of simulated biogas (Figures S6–S10), which can be attributed to the degradation of the catalysts by the sulfur species. Notably, the S 2p peaks were not clearly observed for the spent catalyst pellets because of their low concentrations (Figure S10).

2.4. Reaction Condition Optimization

The reaction conditions were optimized for the best OCM activity to selectively produce C_{2+} compounds (Figure 7) [37,44–47]. The effects of the GHSV, temperature, flow rate, and CH_4/O_2 ratio on CH_4 conversion, C_{2+} selectivity (and yield), olefin selectivity (and yield), and olefin/paraffin ratio were investigated. While the CH_4 conversion depicts the activation of methane to form methyl radicals, the C_{2+} selectivity and the C_{2+} yield depict the formation of methyl radicals rather than the deep oxidation to CO_x . The olefin selectivity increases with improved formation of C_{2+} compounds and improved selective dehydrogenation of paraffins to olefins. The highest CH_4 and O_2 conversions (~16.5% and 100.0%, respectively) were observed at $\text{GHSV} = 3333 \text{ h}^{-1}$, which did not significantly change at $\text{GHSV} < 3333 \text{ h}^{-1}$ (Figure 7a). The dehydrogenation of the paraffins to olefins was improved with increasing space time (decreasing GHSV from 20,000 to 1000 h^{-1}), thereby increasing the olefin selectivity from 37.9% to 54.6%; however, the deep oxidation to CO_x (CO and CO_2) improved, decreasing C_{2+} selectivity.

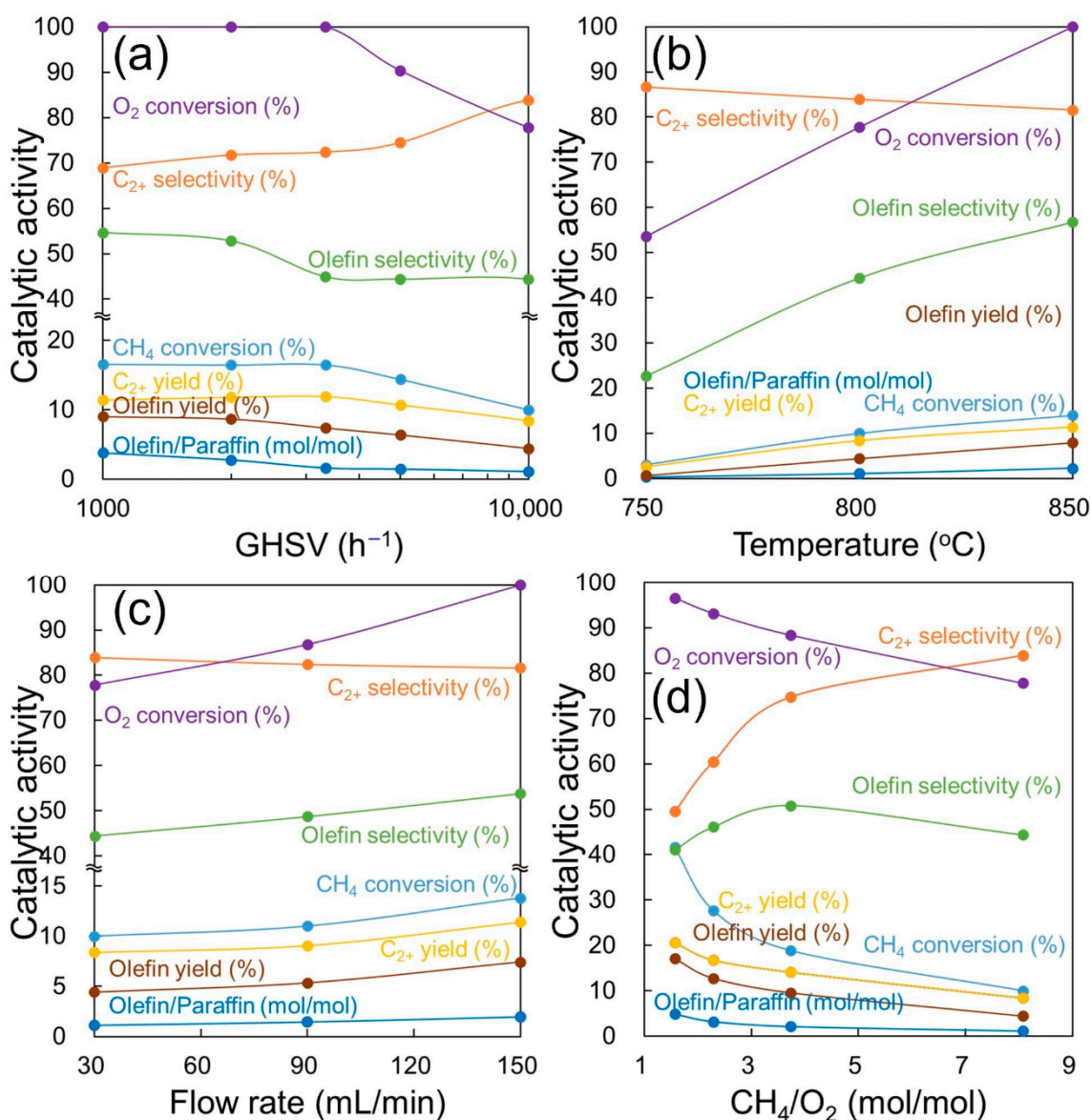


Figure 7. Oxidative coupling of methane results depending on (a) gas hourly space velocity (GHSV), (b) reaction temperature, (c) flow rate, and (d) CH₄/O₂ ratio. Reaction conditions: (a) 800 °C, 30 mL/min of flow rate, and CH₄/O₂/N₂/CO₂/H₂S = 16.1/2/1/10.7/0.1 (v/v/v/v/v). (b) GHSV = 10,000 h⁻¹, 0.18 mL of catalyst, 30 mL/min of flow rate, and CH₄/O₂/N₂/CO₂/H₂S = 16.1/2/1/10.7/0.1 (v/v/v/v/v). (c) GHSV = 10,000 h⁻¹, 0.18 mL of catalyst, 800 °C, and CH₄/O₂/N₂/CO₂/H₂S = 16.1/2/1/10.7/0.1 (v/v/v/v/v). (d) GHSV = 10,000 h⁻¹, 0.18 mL of catalyst, 800 °C, 30 mL/min of flow rate, and (a mixture of CH₄, CO₂, H₂S, and O₂)/N₂ = 29/1 (v/v).

The OCM activity of the catalyst pellets was significantly affected by the reaction temperature (Figure 7b). As the temperature increased from 750 °C to 850 °C, the CH₄ conversion and O₂ conversion increased from 3.01% to 14.0% and 53.6% to 100.0%, respectively. The olefin selectivity also increased from 22.7% (750 °C) to 56.7% (850 °C), while the C₂₊ selectivity decreased from 86.7% (750 °C) to 81.6% (850 °C).

The scale-up of the reaction system was investigated by increasing the flow rate at a fixed GHSV (Figure 7c). The CH₄ and O₂ conversions increased from 10.0% and 77.8% to 13.8% and 100.0%, respectively, as the flow rate increased from 30 to 150 mL/min. However, the C₂₊ selectivity slightly decreased from 83.9% to 81.6%. The trends followed by the effects of the scale-up and reaction temperature are similar, which may be attributed to the formation of hot spots at higher amounts of the catalyst [28].

The OCM activity of the catalyst pellets significantly varied as a result of decreasing CH_4/O_2 ratio (Figure 7d and Table S6). A significant change in catalytic activity was observed at $\text{CH}_4/\text{O}_2 < 3.74$ mol/mol. The CH_4 and O_2 conversions increased from 18.9% and 88.4% to 41.6% and 96.6%, respectively, as the CH_4/O_2 decreased from 8.10 mol/mol to 1.57 mol/mol; however, in the range of 3.74–8.10 mol/mol, the change was minimal. Further, the C_{2+} selectivity decreased from 83.9% to 49.5% with the decreasing CH_4/O_2 ratio, especially from 3.74 mol/mol to 1.57 mol/mol. The olefin selectivity exhibited a volcano-shaped curve, with the highest olefin selectivity (50.8%) at $\text{CH}_4/\text{O}_2 = 3.74$ mol/mol. Although improved dehydrogenation can be expected with a greater amount of the O_2 reactant, the observed lower olefin selectivity at the lower CH_4/O_2 ratio (or the larger amount of O_2) can be attributed to the gas-phase deep oxidation to CO_x .

Based on the results depicted in Figure 7, optimized reaction conditions were determined (Figure 8). Increasing the reaction temperature and decreasing the CH_4/O_2 ratio increased the CH_4 conversion but decreased C_{2+} selectivity. The C_{2+} yield, a product of CH_4 conversion and C_{2+} selectivity, also increased with increasing the reaction temperature and decreasing the CH_4/O_2 ratio. This suggests that CH_4 conversion is a more decisive variable for the C_{2+} yield. The olefin selectivity exhibited a complex dependence on the temperature and CH_4/O_2 ratio because the formation of olefins requires the production of paraffins (C_{2+} yield). Based on the suggested facile process operation, the optimal reaction conditions of 800 °C and $\text{CH}_4/\text{O}_2 = 8.10$ mol/mol were selected, and a long-term OCM of simulated biogas was performed for 100 h. No significant catalyst deactivation (Figure 9) or change in the catalyst pellets after 100 h of reaction were observed (Figure S11).

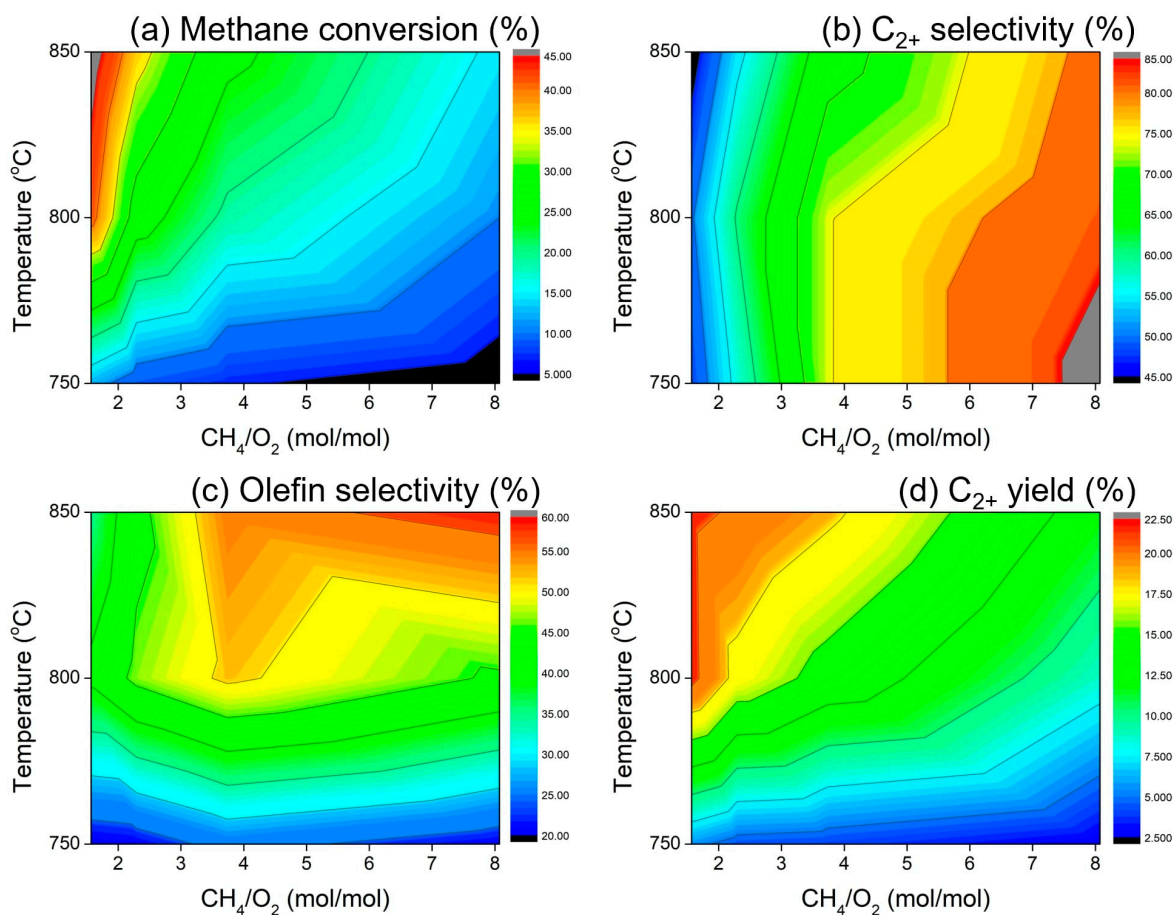


Figure 8. Optimization of the CH_4/O_2 ratio and temperature for the oxidative coupling of methane activity. (a) CH_4 conversion, (b) C_{2+} selectivity, (c) Olefin selectivity, (d) C_{2+} yield.

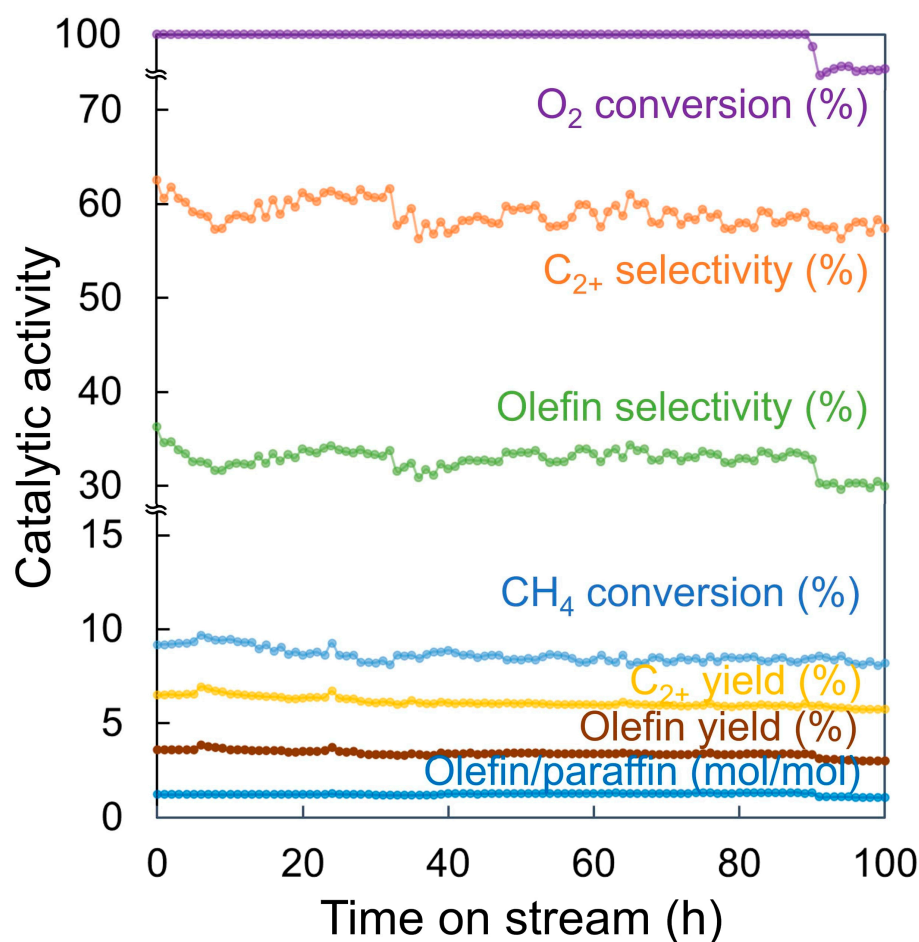


Figure 9. Long-term oxidative coupling of methane results of simulated biogas using N(8)M(0.5)P(1.5).

3. Experimental Section

3.1. Materials

All chemicals were used without further purification. MC (viscosity = 4000 cP), Mont (K10, powder), titanium oxide (TiO₂ P25, ≥99.5%), starch (soluble ACS reagent), and poly(vinyl alcohol) (PVA, M.W. = 89,000–98,000, 99+% hydrolyzed) were purchased from Sigma-Aldrich (Milwaukee, WI, USA). Aluminum oxide (Al₂O₃, γ-phase, 99.97%) and magnesium oxide (MgO, 96%, heavy) were purchased from Alfa Aesar (Ward Hill, Haverhill, MA, USA). Sodium tungstate dihydrate (Na₂WO₄·2H₂O) was purchased from Junsei Chemicals (Tokyo, Japan). Manganese nitrate hexahydrate (Mn(NO₃)₂·6H₂O, 98%) was purchased from Kanto Chemicals (Tokyo, Japan). Methane (CH₄, 99.97%), a mixture of methane, carbon dioxide, and hydrogen sulfide (CH₄/CO₂/H₂S = 59.7/39.8/0.5 (v/v/v)), oxygen (O₂, 99.5%), helium (He, 99.999%), hydrogen (H₂, 99.999%), ethane (C₂H₆, 99.5%), and ethylene (C₂H₄, 99.99%) were purchased from Shinyang Air (Seoul, Korea). Deionized (DI) water (18.2 MΩ·cm) was prepared using an aqua MAX-Ultra 370 series water purification system (YL Instruments, Anyang, Korea).

3.2. Catalyst Preparation

3.2.1. Na₂WO₄/Mn/SiO₂ (NWM) Catalyst

The Na₂WO₄ (5 wt %)/Mn (2 wt %)/SiO₂ catalyst was prepared using the wetness impregnation method. The silica support (100 g) was dispersed in DI water (300 mL) and stirred for 30 min. Na₂WO₄·2H₂O (6.014 g) and Mn(NO₃)₂·6H₂O (6.42 mL) were added to the mixture and stirred for 3 h. The solution was dried in air at 105 °C and calcined at 800 °C for 5 h.

3.2.2. Catalyst Pellets

The catalyst pellets were prepared using an extrusion method. The catalyst powder (8 g) was mixed with inorganic binders (0–6 g), organic binders (0–2 g), and DI water (6–10 mL). The mixture was kneaded for 5–10 min, and the prepared paste was extruded with a diameter of 2 mm. The extrudates were cut into 3–5 mm long pellets, which were dried at 105 °C for 16 h and calcined at 800 °C for 6 h. Details of the pellet preparation method are provided in Table S6.

3.3. Catalytic Activity Measurement

Catalytic activity was measured using a packed-bed quartz I-tube reactor with an internal diameter of 6 mm and a 250 mm straight cylindrical tubing. A mid-scale reaction was conducted using a reactor with an internal diameter of 1.54 cm. The catalyst bed was placed between the quartz wool in the middle of the reactor. Zirconia–silica ceramic beads, which are inert during OCM, filled the remainder of the reactor volume. The flow rates were controlled using mass-flow controllers. The total flow rate was 30–150 mL/min. The GHSV was controlled by increasing the amount of the catalyst from 1000 to 20,000 h⁻¹. Prior to the reaction, the catalyst was pretreated under N₂ flow by heating to 700 °C at a heating rate of 10 °C/min and maintained for 60 min. The reaction was performed at 700–850 °C. The temperature was maintained for 30 min prior to GC injection, followed by ramping at 5 °C/min. The flow rates were controlled using mass-flow controllers. The reaction mixture, including CH₄, O₂, CO, CO₂, C₂H₂, C₂H₄, C₂H₆, C₃H₆, and C₃H₈, was identified using a flame ionization detector (FID) and a thermal conductivity detector (TCD). O₂, CO, and CO₂ were quantified using a TCD with a 60/80 Carboxen-1000 packed column, and CH₄, C₂, and C₃ hydrocarbons were analyzed using the FID with an Agilent 19091P-S15 column. N₂ was used as the internal standard. Selectivity, conversion, and yield were calculated based on the data collected after 30 min of reaction (Equations (1)–(3)). The reaction was performed three times and averaged, which exhibited a deviation of ~3.7% CH₄ conversion.

$$\text{Conversion (\%)} = (\text{consumed moles of methane}) / (\text{initial moles of methane}) \times 100 \quad (1)$$

$$\text{Selectivity of } C_xH_yO_z \text{ (\%)} = x \times (\text{produced moles of } C_xH_yO_z) / (\text{consumed moles of methane}) \times 100 \quad (2)$$

$$\text{Yield of } C_xH_yO_z \text{ (\%)} = x \times (\text{produced moles of } C_xH_yO_z) / (\text{initial moles of methane}) \times 100 \quad (3)$$

3.4. Catalyst Characterization

N₂ physisorption was performed using an ASAP 2020 device (Micromeritics, Norcross, GA, USA). The fracture strength of the pellets was measured using an AFG-100N digital force gauge (Mecmesin, Slinfold, England). The pellet was loaded between the horizontally placed anvils with each end clamped. The magnitude of load where fracture of the pellet occurred was recorded. The value was divided by the cross-sectional area of pellet. Because the length of extruded pellets was not the same but ranged 3 to 5 mm, 20 catalyst pellets were measured, and the results were averaged. SEM images were collected using an Inspect F field-emission scanning electron microscope (Thermo Fisher Scientific, Waltham, MA, USA). O₂ TPD was performed using a BELCAT-B catalyst analyzer (MicrotracBEL, Osaka, Japan) equipped with a TCD and a mass spectrometer. Powder XRD was performed using a Dmax2500-PC (RIGAKU, Tokyo, Japan) with Cu K α ₁ radiation ($\lambda = 1.5406 \text{ \AA}$, 40 kV, and 200 mA). All samples were crushed into powder form prior to the XRD measurement. XRD data were collected using a quartz holder at $2\theta = 5\text{--}90^\circ$ with a step scan rate of 4°/min. XPS was performed using a Theta Probe AR-XPS system (Thermo Fisher Scientific, Waltham, MA, USA) with monochromated Al K α excitation ($h\nu = 1486.6 \text{ eV}$) operated at 15 kV and 150 W at the Korea Basic Science Institute (Busan, Korea). The measured binding energy was calibrated using the C 1s peak at 284.6 eV. High-temperature powder XRD was conducted using an X'Pert PRO (Philips, Amsterdam, Netherlands) with Cu K α ₁ radiation ($\lambda = 1.5406 \text{ \AA}$, 60 kV, and 60 mA).

3.5. Calculation of Higher Heat Values (HHV)

The higher heating value (HHV) of the product stream was calculated using the molar fractions of the hydrocarbons and the corresponding HHV values in MJ/Nm³ under standard conditions for temperature and pressure (Table S7). The molar fractions (x_i) of the hydrocarbons were measured using the GC results. Only the hydrocarbon mixtures without CO, CO₂, O₂, and other compounds were used to calculate the total HHV (HHV_{total}) (Equation (4)) [49].

$$\text{HHV}_{\text{total}} = \sum x_i \text{HHV}_i \quad (4)$$

4. Conclusions

The catalytic OCM reaction was observed in different reaction systems for developing scaled-up biogas upgrading processes. The HHV increased from 39.9 (CH₄, Wobbe index = 53.5 MJ/Nm³) to 41.0 MJ/Nm³ (OCM product mixture, Wobbe index = 54.2 MJ/Nm³), achieving the fuel standard prescribed in many countries (Wobbe index = 45.5–55.0 MJ/Nm³). The type and compositions of the organic/inorganic binders widely influenced the physical properties, such as morphology, specific surface area, and fracture strength, of the catalyst pellets. The effect of the organic/inorganic binders on the catalytic activity was also examined. The inorganic binder affected the catalytic activity or crystalline structure of the pellets by supplying O₂ to the active sites, while the organic binder affected the catalytic activity of NWM by mediating the interaction between the catalyst and the inorganic binder. The sensitivity of the reaction parameters (temperature, GHSV, total flow rate, and CH₄/O₂ ratio) was also examined. The reaction conditions were optimized based on the results of the sensitivity analysis. Furthermore, the stable OCM activity of NWM was confirmed by the results of a long-term (100 h) operation. Because this study focused on the preparation of catalyst pellets and the process condition optimization using these pellets, we provided the preliminary knowledge to design the scaled-up biogas upgrading process. Although the observed reaction results indicated that the scale up process did not significantly adjust the catalytic activity, an experimental confirmation was required to verify the optimized conditions of biogas upgrading processes. A better understanding of scaled-up OCM processes of biogas upgrades may be achieved based on the findings in this study because the process analyses in the literature are based on the OCM results of a powder catalyst without the sulfur-containing compounds in the reaction feed.

Supplementary Materials: The following are available online at <https://www.mdpi.com/article/10.3390/catal11111301/s1>, Table S1: Higher heating values of OCM products in STP conditions, Table S2: Compositions of OCM products, Table S3: OCM results at 800 °C using catalyst pellets depending on organic binders, Table S4: OCM results at 800 °C using inorganic binders, Table S5: OCM results at 800 °C using catalyst pellets depending on inorganic binders with different feed composition, Table S6: Preparation of catalyst pellets, Table S7: Higher heating values of products at STP conditions, Figure S1: O₂ TPD results of fresh catalyst pellets depending on the fractions of (a) inorganic binder P25 and (b) organic binder MC, Figure S2: Powder XRD results of (a) fresh and (b) spent catalyst pellets depending on organic binders, Figure S3: Powder XRD results of fresh N(8)M(0.5)P(1.5) depending on the calcination environments of air, N₂, and 5% H₂/Ar, Figure S4: TEM-EDS result of spent N(8)M(0.5)P(1.5), Figure S5: Powder XRD results of (a) fresh and (b) spent catalyst pellets depending on the amount of inorganic binder P25, Figure S6: Na 1s XPS results of (a) fresh and (b) spent catalyst pellets depending on inorganic binders, Figure S7: Mn 2p XPS results of (a) fresh and (b) spent catalyst pellets depending on inorganic binders, Figure S8: Si 2p XPS results of (a) fresh and (b) spent catalyst pellets depending on inorganic binders, Figure S9: O 1s XPS results of (a) fresh and (b) spent catalyst pellets depending on inorganic binders, Figure S10: S 2p XPS results of (a) fresh and (b) spent catalyst pellets depending on inorganic binders, Figure S11: Powder XRD results of spent catalysts after 100 h reaction.

Author Contributions: Conceptualization, S.G. and J.-M.H.; methodology, S.G.; validation, J.-W.C., D.J.S. and C.-J.Y.; formal analysis, S.G. and J.-W.C.; investigation, S.G. and J.-M.H.; writing—original draft preparation, S.G. and J.-M.H.; writing—review and editing, J.C. and J.-M.H.; supervision,

D.J.S., C.-J.Y., J.C. and J.-M.H.; funding acquisition, J.-M.H. All authors have read and agreed to the published version of the manuscript.

Funding: This research was funded by the C1 Gas Refinery Program (2015M3D3A1A01064900) and the Technology Development Program to Solve Climate Changes (2020M1A2A2079798) through the National Research Foundation of Korea (NRF) funded by the Ministry of Science and ICT.

Acknowledgments: This research was supported by the C1 Gas Refinery Program (2015M3D3A1A01064900) and the Technology Development Program to Solve Climate Changes (2020M1A2A2079798) through the National Research Foundation of Korea (NRF) funded by the Ministry of Science and ICT.

Conflicts of Interest: The authors declare no conflict of interest.

References

- Holm-Nielsen, J.B.; Al Seadi, T.; Oleskowicz-Popiel, P. The future of anaerobic digestion and biogas utilization. *Bioresour. Technol.* **2009**, *100*, 5478–5484. [CrossRef]
- Hoyer, K.; Hultheberg, C.; Svensson, M.; Jernberg, J.; Nörregård, Ö. *Biogas Upgrading-Technical Review*; Report; Energiforsk: Stockholm, Sweden, 2016. Available online: http://vav.griffel.net/filer/C_Energiforsk2016-275.pdf (accessed on 6 October 2021).
- Scarlat, N.; Dallemand, J.-F.; Fahl, F. Biogas: Developments and perspectives in Europe. *Renew. Energy* **2018**, *129*, 457–472. [CrossRef]
- Achinas, S.; Achinas, V.; Euverink, G.J.W. A Technological Overview of Biogas Production from Biowaste. *Engineering* **2017**, *3*, 299–307. [CrossRef]
- Paolini, V.; Petracchini, F.; Segreto, M.; Tomassetti, L.; Naja, N.; Cecinato, A. Environmental impact of biogas: A short review of current knowledge. *J. Environ. Sci. Health Part A* **2018**, *53*, 899–906. [CrossRef]
- Adnan, A.I.; Ong, M.Y.; Nomanbhay, S.; Chew, K.W.; Show, P.L. Technologies for biogas upgrading to biomethane: A review. *Bioengineering* **2019**, *6*, 92. [CrossRef]
- Gustafsson, M.; Ammenberg, J.; Murphy, J.D. *IEA Bioenergy Task 37—Country Reports Summaries 2019*; Report; IEA Bioenergy: Paris, France, 2020. Available online: <https://task37.ieabioenergy.com/country-reports.html> (accessed on 6 October 2021).
- Association, E.B. *EBA Statistical Report 2018*; Annual Report; European Biogas Association: Brussels, Belgium, 2018.
- Bharathiraja, B.; Sudharsanaa, T.; Bharghavi, A.; Jayamuthunagai, J.; Praveenkumar, R. Biohydrogen and Biogas—An overview on feedstocks and enhancement process. *Fuel* **2016**, *185*, 810–828. [CrossRef]
- Anukam, A.; Mohammadi, A.; Naqvi, M.; Granström, K. A review of the chemistry of anaerobic digestion: Methods of accelerating and optimizing process efficiency. *Processes* **2019**, *7*, 504. [CrossRef]
- Petersson, A.; Wellinger, A. Biogas upgrading technologies—developments and innovations. *IEA Bioenergy* **2009**, *20*, 1–19.
- Angelidaki, I.; Treu, L.; Tsapekos, P.; Luo, G.; Campanaro, S.; Wenzel, H.; Kougias, P.G. Biogas upgrading and utilization: Current status and perspectives. *Biotechnol. Adv.* **2018**, *36*, 452–466. [CrossRef] [PubMed]
- Penteado, A.T.; Kim, M.; Godini, H.R.; Esche, E.; Repke, J.-U. Biogas as a renewable feedstock for green ethylene production via oxidative coupling of methane: Preliminary feasibility study. *Chem. Eng. Trans.* **2017**, *61*, 589–594.
- Penteado, A.T.; Kim, M.; Godini, H.R.; Esche, E.; Repke, J.-U. Techno-economic evaluation of a biogas-based oxidative coupling of methane process for ethylene production. *Front. Chem. Sci. Eng.* **2018**, *12*, 598–618. [CrossRef]
- Sokolov, S.; Seeburg, D.; Wohlrab, S.; Friedel, M.; Nitzsche, J.; Kondratenko, E.V. An Approach Using Oxidative Coupling of Methane for Converting Biogas and Acid Natural Gas into High-Calorific Fuels. *Ind. Eng. Chem. Res.* **2019**, *58*, 2454–2459. [CrossRef]
- Gu, S.; Choi, J.-W.; Suh, D.J.; Park, Y.-K.; Choi, J.; Ha, J.-M. Upgrading of sulfur-containing biogas into high quality fuel via oxidative coupling of methane. *Int. J. Energy Res.* **2021**, *45*, 19363–19377. [CrossRef]
- Kondratenko, E.V.; Schluter, M.; Baerns, M.; Linke, D.; Holena, M. Developing catalytic materials for the oxidative coupling of methane through statistical analysis of literature data. *Catal. Sci. Technol.* **2015**, *5*, 1668–1677. [CrossRef]
- Gambo, Y.; Jalil, A.A.; Triwahyono, S.; Abdurashed, A.A. Recent advances and future prospect in catalysts for oxidative coupling of methane to ethylene: A review. *J. Ind. Eng. Chem.* **2018**, *59*, 218–229. [CrossRef]
- Fang, X.; Li, S.; Lin, J.; Chu, Y. Oxidative coupling of methane on W-Mn catalysts. *J. Mol. Catal.* **1992**, *6*, 427–433.
- Pak, S.; Lunsford, J.H. Thermal effects during the oxidative coupling of methane over Mn/Na₂WO₄/SiO₂ and Mn/Na₂WO₄/MgO catalysts. *Appl. Catal. A Gen.* **1998**, *168*, 131–137. [CrossRef]
- Malekzadeh, A.; Khodadadi, A.; Abedini, M.; Amini, M.; Bahramian, A.; Dalai, A.K. Correlation of electrical properties and performance of OCM MO_x/Na₂WO₄/SiO₂ catalysts. *Catal. Commun.* **2001**, *2*, 241–247. [CrossRef]
- Arndt, S.; Otremba, T.; Simon, U.; Yildiz, M.; Schubert, H.; Schomäcker, R. Mn–Na₂WO₄/SiO₂ as catalyst for the oxidative coupling of methane. What is really known? *Appl. Catal. A Gen.* **2012**, *425–426*, 53–61. [CrossRef]
- Blanksby, S.J.; Ellison, G.B. Bond Dissociation Energies of Organic Molecules. *Acc. Chem. Res.* **2003**, *36*, 255–263. [CrossRef]
- Takanabe, K.; Iglesia, E. Mechanistic aspects and reaction pathways for oxidative coupling of methane on Mn/Na₂WO₄/SiO₂ catalysts. *J. Phys. Chem. C* **2009**, *113*, 10131–10145. [CrossRef]

25. Lee, M.; Park, M.-J.; Jeon, W.; Choi, J.-W.; Suh, Y.-W.; Suh, D.J. PLS-based kinetics modeling and optimization of the oxidative coupling of methane over Na₂WO₄/Mn/SiO₂ catalyst. *Korean J. Chem. Eng.* **2011**, *28*, 2142–2147. [[CrossRef](#)]
26. Lee, M.R.; Park, M.J.; Jeon, W.; Choi, J.W.; Suh, Y.W.; Suh, D.J. A kinetic model for the oxidative coupling of methane over Na₂WO₄/Mn/SiO₂. *Fuel Process. Technol.* **2012**, *96*, 175–182. [[CrossRef](#)]
27. Kiani, D.; Sourav, S.; Wachs, I.E.; Baltrusaitis, J. Synthesis and molecular structure of model silica-supported tungsten oxide catalysts for oxidative coupling of methane (OCM). *Catal. Sci. Technol.* **2020**, *10*, 3334–3345. [[CrossRef](#)]
28. Lee, J.Y.; Jeon, W.; Choi, J.-W.; Suh, Y.-W.; Ha, J.-M.; Suh, D.J.; Park, Y.-K. Scaled-up production of C₂ hydrocarbons by the oxidative coupling of methane over pelletized Na₂WO₄/Mn/SiO₂ catalysts: Observing hot spots for the selective process. *Fuel* **2013**, *106*, 851–857. [[CrossRef](#)]
29. Zhao, X.; Stachurski, P.; Shah, S.; Maiti, D.; Ramani, S.; Wright, A.; Walker, D.; Joseph, B.; Kuhn, J.N. Design and optimization of NiMg/ceria-zirconia catalyst pellets. *Powder Technol.* **2019**, *357*, 214–222. [[CrossRef](#)]
30. Baldovino-Medrano, V.G.; Le, M.T.; Van Driessche, I.; Bruneel, E.; Alcázar, C.; Colomer, M.T.; Moreno, R.; Florencie, A.; Farin, B.; Gaigneaux, E.M. Role of shaping in the preparation of heterogeneous catalysts: Tableting and slip-casting of oxidation catalysts. *Catal. Today* **2015**, *246*, 81–91. [[CrossRef](#)]
31. Hernando, H.; Ochoa-Hernández, C.; Shamzhy, M.; Moreno, I.; Feroso, J.; Pizarro, P.; Coronado, J.M.; Čejka, J.; Serrano, D.P. The crucial role of clay binders in the performance of ZSM-5 based materials for biomass catalytic pyrolysis. *Catal. Sci. Technol.* **2019**, *9*, 789–802. [[CrossRef](#)]
32. Nevalainen, P.; Kinnunen, N.; Suvanto, M. Developmental Study of Soot-Oxidation Catalysts for Fireplaces: The Effect of Binder and Preparation Techniques on Catalyst Texture and Activity. *Catalysts* **2019**, *9*, 957. [[CrossRef](#)]
33. Seo, J.-H.; Chae, H.-J.; Kim, T.-W.; Jeong, K.-E.; Kim, C.-U.; Lee, S.-B.; Jeong, S.-Y. Influence of Binder on Fe-based Extrudate as Fischer-Tropsch Catalysts. *Korean Chem. Eng. Res.* **2011**, *49*, 726–731. [[CrossRef](#)]
34. Palermo, A.; Holgado Vazquez, J.P.; Lee, A.F.; Tikhov, M.S.; Lambert, R.M. Critical influence of the amorphous silica-to-cristobalite phase transition on the performance of Mn/Na₂WO₄/SiO₂ catalysts for the oxidative coupling of methane. *J. Catal.* **1998**, *177*, 259–266. [[CrossRef](#)]
35. Ji, S.-F.; Xiao, T.-C.; Li, S.-B.; Xu, C.-Z.; Hou, R.-L.; Coleman, K.S.; Green, M.L.H. The relationship between the structure and the performance of Na-W-Mn/SiO₂ catalysts for the oxidative coupling of methane. *Appl. Catal. A Gen.* **2002**, *225*, 271–284. [[CrossRef](#)]
36. Nipan, G.D. Melt-assisted phase transformations of A/W/Mn/SiO₂ (A = Li, Na, K, Rb, Cs) composite catalysts. *Inorg. Mater.* **2017**, *53*, 553–559. [[CrossRef](#)]
37. Jeon, W.; Lee, J.Y.; Lee, M.; Choi, J.-W.; Ha, J.-M.; Suh, D.J.; Kim, I.W. Oxidative coupling of methane to C₂ hydrocarbons on the Mg–Ti mixed oxide-supported catalysts at the lower reaction temperature: Role of surface oxygen atoms. *Appl. Catal. A Gen.* **2013**, *464–465*, 68–77. [[CrossRef](#)]
38. Wang, P.; Zhao, G.; Liu, Y.; Lu, Y. TiO₂-doped Mn₂O₃-Na₂WO₄/SiO₂ catalyst for oxidative coupling of methane: Solution combustion synthesis and MnTiO₃-dependent low-temperature activity improvement. *Appl. Catal. A Gen.* **2017**, *544*, 77–83. [[CrossRef](#)]
39. Gu, S.; Oh, H.-S.; Choi, J.-W.; Suh, D.J.; Jae, J.; Choi, J.; Ha, J.-M. Effects of metal or metal oxide additives on oxidative coupling of methane using Na₂WO₄/SiO₂ catalysts: Reducibility of metal additives to manipulate the catalytic activity. *Appl. Catal. A Gen.* **2018**, *562*, 114–119. [[CrossRef](#)]
40. Lim, S.; Choi, J.-W.; Suh, D.J.; Song, K.H.; Ham, H.C.; Ha, J.-M. Combined experimental and density functional theory (DFT) studies on the catalyst design for the oxidative coupling of methane. *J. Catal.* **2019**, *375*, 478–492. [[CrossRef](#)]
41. Fleischer, V.; Simon, U.; Parishan, S.; Colmenares, M.G.; Görke, O.; Gurlo, A.; Riedel, W.; Thum, L.; Schmidt, J.; Risse, T.; et al. Investigation of the role of the Na₂WO₄/Mn/SiO₂ catalyst composition in the oxidative coupling of methane by chemical looping experiments. *J. Catal.* **2018**, *360*, 102–117. [[CrossRef](#)]
42. Werny, M.J.; Wang, Y.; Girgsdies, F.; Schlögl, R.; Trunschke, A. Fluctuating storage of the active phase in a Mn-Na₂WO₄/SiO₂ catalyst for the oxidative coupling of methane. *Angew. Chem. Int. Ed.* **2020**, *59*, 14921–14926. [[CrossRef](#)] [[PubMed](#)]
43. Vandewalle, L.A.; Van de Vijver, R.; Van Geem, K.M.; Marin, G.B. The role of mass and heat transfer in the design of novel reactors for oxidative coupling of methane. *Chem. Eng. Sci.* **2019**, *198*, 268–289. [[CrossRef](#)]
44. Yoon, S.; Lim, S.; Choi, J.-W.; Suh, D.J.; Song, K.H.; Ha, J.-M. Study on the unsteady state oxidative coupling of methane: Effects of oxygen species from O₂, surface lattice oxygen, and CO₂ on the C₂₊ selectivity. *RSC Adv.* **2020**, *10*, 35889–35897. [[CrossRef](#)]
45. Mleczko, L.; Baerns, M. Catalytic oxidative coupling of methane—Reaction engineering aspects and process schemes. *Fuel Process. Technol.* **1995**, *42*, 217–248. [[CrossRef](#)]
46. Ohyama, J.; Nishimura, S.; Takahashi, K. Data Driven Determination of Reaction Conditions in Oxidative Coupling of Methane via Machine Learning. *ChemCatChem* **2019**, *11*, 4307–4313. [[CrossRef](#)]
47. Hayek, N.S.; Khlief, G.J.; Horani, F.; Gazit, O.M. Effect of reaction conditions on the oxidative coupling of methane over doped MnO_x-Na₂WO₄/SiO₂ catalyst. *J. Catal.* **2019**, *376*, 25–31. [[CrossRef](#)]
48. Damby, D.E.; Llewellyn, E.W.; Horwell, C.J.; Williamson, B.J.; Najorka, J.; Cressey, G.; Carpenter, M. The α-β phase transition in volcanic cristobalite. *J. Appl. Cryst.* **2014**, *47*, 1205–1215. [[CrossRef](#)] [[PubMed](#)]
49. Linstrom, P.; Mallard, W. NIST Chemistry Webbook. NIST Standard Reference Database. 2021. Available online: <http://webbook.nist.gov/chemistry> (accessed on 18 August 2021).